Title

A segmentation and point-matching enhanced efficient deformable image registration method for dose accumulation between HDR CT images

Journal

Physics in Medicine and Biology, 60(7)

ISSN

0031-9155

Authors

Zhen, Xin
Chen, Haibin
Yan, Hao
et al.

Publication Date

2015-04-07

DOI

10.1088/0031-9155/60/7/2981

Peer reviewed

A segmentation and point-matching enhanced efficient deformable image registration method for dose accumulation between HDR CT images

2015 Phys. Med. Biol. 60 2981

(http://iopscience.iop.org/0031-9155/60/7/2981)

IOP Publishing | Institute of Physics and Engineering in Medicine Physics in Medicine & Biology

Phys. Med. Biol. **60** (2015) 2981–3002 doi:10.1088/0031-9155/60/7/2981

A segmentation and point-matching enhanced efficient deformable image registration method for dose accumulation between HDR CT images

Xin Zhen[1], Haibin Chen[1], Hao Yan[2], Linghong Zhou[1], Loren K Mell[3], Catheryn M Yashar[3], Steve Jiang[2], Xun Jia[2], Xuejun Gu[2] and Laura Cervino[3]

[1] Department of Biomedical Engineering, Southern Medical University, Guangzhou, Guangdong 510515, People's Republic of China
[2] Department of Radiation Oncology, The University of Texas, Southwestern Medical Center, Dallas, Texas 75390, USA
[3] Center for Advanced Radiotherapy Technologies and Department of Radiation Medicine and Applied Sciences, University of California San Diego, La Jolla, CA 92037-0843, USA

E-mail: lcervino@ucsd.edu and smart@smu.edu.cn

Received 22 October 2014, revised 21 January 2015
Accepted for publication 1 February 2015
Published 19 March 2015

Abstract

Deformable image registration (DIR) of fractional high-dose-rate (HDR) CT images is challenging due to the presence of applicators in the brachytherapy image. Point-to-point correspondence fails because of the undesired deformation vector fields (DVF) propagated from the applicator region (AR) to the surrounding tissues, which can potentially introduce significant DIR errors in dose mapping. This paper proposes a novel *segmentation and point-matching enhanced efficient DIR* (named SPEED) scheme to facilitate dose accumulation among HDR treatment fractions. In SPEED, a semi-automatic seed point generation approach is developed to obtain the incremented fore/background point sets to feed the random walks algorithm, which is used to segment and remove the AR, leaving empty AR cavities in the HDR CT images. A feature-based 'thin-plate-spline robust point matching' algorithm is then employed for AR cavity surface points matching. With the resulting mapping, a DVF defining on each voxel is estimated by B-spline approximation, which serves as the initial DVF for the subsequent Demons-based DIR between the AR-free HDR CT images. The calculated DVF via Demons combined with the initial one serve as the final DVF to map doses between HDR fractions. The segmentation and registration accuracy are

quantitatively assessed by nine clinical HDR cases from three gynecological cancer patients. The quantitative analysis and visual inspection of the DIR results indicate that SPEED can suppress the impact of applicator on DIR, and accurately register HDR CT images as well as deform and add interfractional HDR doses.

Keywords: deformable registration, brachytherapy, gynecological cancer, medical physics

(Some figures may appear in colour only in the online journal)

1. Introduction

Radiation therapy is an effective treatment modality for gynecological cancer. The curative potential of radiation therapy in the management of gynecological cancer is greatly enhanced by the use of high-dose-rate (HDR) brachytherapy, which often serves as a boost for external beam radiotherapy (EBRT) (Trimble *et al* 2008, Pearce *et al* 2009, Han *et al* 2013). Clinical outcomes are related to the planning target volume (PTV) and organ dose over multi-fractional treatment (Christensen *et al* 2001, Vasquez Osorio *et al* 2011, Sabater *et al* 2013). Due to inter-fractional patient geometry variation, accurate organ dose reporting is a non-trivial task.

Deformable image registration (DIR) provides means for accumulating physical or biological dose at tissue voxel level, which theoretically can predict accurate dose absorption and patient's response to a course of treatment. Since clinical use of brachytherapy always involves the placement of an intracavitary applicator, the DIR between HDR fractional CT images therefore becomes a challenging problem. Firstly, the insertion of an applicator will change the geometry of surrounding tissues dramatically, producing secondary deformation that further heightens the inter-fractional anatomic changes (Christensen *et al* 2001, Sabater *et al* 2013). For this reason, the DIR is required to be capable of accommodating large tissue deformations. Secondly, the sharp dose gradient of 5 ~ 12% per mm characteristic of intracavitary brachytherapy (Anderson *et al* 2013) calls for accurate deformation vector field (DVF) for reducing dose accumulation uncertainty (Salguero *et al* 2011, Murphy *et al* 2012). Thirdly, as an external object, the applicator moves independently and inconsistently relative to the surrounding tissues, which potentially violates the smoothness constraint of the DVF enforced by most DIR algorithms (Crum *et al* 2004, Holden 2008). In addition, it was found that the applicator position within the patient body varies dramatically between different HDR insertions, and the average applicator shift can be up to 1.0 ~ 1.5 cm posteriorly and inferiorly from one insertion to the next (Grigsby *et al* 1993), which cannot be ignored. As a consequence, the relatively large DVF calculated inside the applicator region (AR) is likely to be propagated to its surrounding tissues by the DVF smoothing operation in DIR, affecting tissues' registration and dose summation accuracy. Furthermore, if different types of applicators are used for a same patient, DIR between two HDR CT images with different applicators will violate the fundamental assumption of most DIR algorithms that there should be one-to-one correspondence for every voxel in the two images to be registered (Crum *et al* 2004, Holden 2008, Zhen *et al* 2013).

To avoid the influence of applicator on DIR, Christensen *et al* (2001) proposed a DIR scheme to match several manual contoured organ boundaries instead of the gray-scale image by modeling the tissue deformation as a viscous-fluid. Vasquez Osorio *et al* (2011) developed a method for adding dose distributions of EBRT and brachytherapy for oropharyngeal patients. This method also involves a manual delineation of a couple of the structures' surface

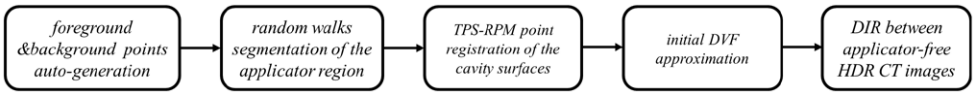

Figure 1. Workflow of SPEED.

in both CT scans, then a thin-plate spline based non-rigid DIR algorithm is used to register the two structure sets to generate a smooth spatial mapping for dose accumulation. The limitation of these approaches is that only organs' boundaries, rather than all the intensity information of the organs, are extracted for registration, thus, tissue deformation inside the contoured organs is not necessarily accurately estimated, even though the organs' boundaries are well matched. Furthermore, manual placement of landmarks and segmentation are time consuming steps, which may potentially introduce another source of error.

In this work, we propose and validate a novel *segmentation and point-matching enhanced efficient DIR* algorithm (named SPEED) for accurate DIR facilitating dose accumulation among HDR treatment fractions in gynecological brachytherapy. Nine clinical HDR cases from three gynecological cancer patients are used for performance evaluation. It is found that SPEED can suppress the influence of the applicator and yield accurate registration results between fractional HDR CT images.

2. Methods and materials

Figure 1 illustrates the workflow of SPEED. A seed-points generation step is developed to auto-generate foreground and background points for the random walks algorithm (Grady 2006), which is used to accurately segment and remove the applicator region (AR), leaving empty cavities in the HDR CT images. A feature-based 'thin-plate-spline robust point matching' (TPS-RPM) algorithm (Chui and Rangarajan 2003, Yang 2011) is then utilized for cavity surface point matching. The DVF defined on each voxel that is characteristic of the deformation between the cavity surfaces is generated by B-spline approximation, and adopted as the initial DVF for the subsequent Demons DIR between the applicator-free HDR CT images. Key steps of the SPEED algorithm will be detailed in section 2.1–2.5.

2.1. Review of the random walks algorithm

Segmentation of the AR in HDR CT images is accomplished by random walks algorithm (Grady 2006), which solves the segmentation problem by calculating the probability that a random walker starting at each unlabeled voxel will first reach one of the given user-defined labels. Let us denote the static and moving HDR fraction CT images as $\boldsymbol{I}_s$ and $\boldsymbol{I}_m$ (with size $X \times Y \times Z$), respectively. For simplicity, $\boldsymbol{I}$ is used to represent $\boldsymbol{I}_s$ and $\boldsymbol{I}_m$. In this approach, a graph $G = (V, E)$, with a fixed number of vertices V and edges E, is first created based on image $\boldsymbol{I}$. The connectivity of two adjacent vertices v_i and v_j ($v \in V$) on an edge e_{ij} ($e \in E$) is weighted by $\omega_{ij} = \exp(-\beta(g_i - g_j)^2)$, where g_i indicates the image intensity at voxel i and β is a free parameter to adjust weight. The desired random walker probabilities can be obtained by solving the following combinatorial Dirichlet function:

$$D[x] = \frac{1}{2}x^T L x = \frac{1}{2}\sum_{e_{ij}\in E}\omega_{ij}(x_i - x_j)^2 \tag{1}$$

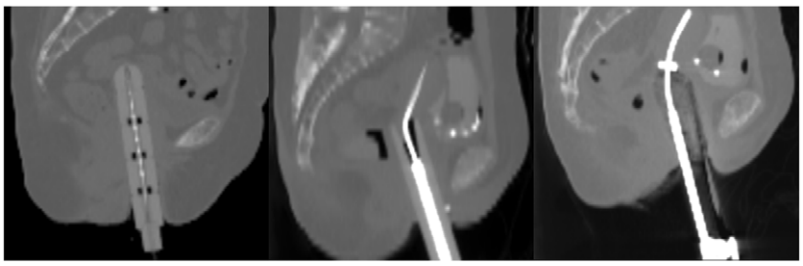

Figure 2. Cylinder (left), cylinder and tandem (middle) and tandem and ovoids (right) applicator used in HDR.

where L is a sparse Laplacian matrix that can be partitioned into four sub-matrices:

$$\begin{bmatrix} L_M & B \\ B^T & L_U \end{bmatrix}, \tag{2}$$

where the subscripts M and U stand for labeled and unlabeled voxels. The probabilities for those unlabeled voxels can be easily calculated by solving a sparse, positive-definite linear equation by differentiating equation (1):

$$L_U x_U = -B^T x_M. \tag{3}$$

where x_M and x_U correspond to the probilities of the labeled and unlabeled voxels respectively. Denoting the probability assumed at vertex v_i, for each label s, by x_i^s, the final segmentation is obtained by assigning each vertex v_i the label corresponding to maximum probability $\max_s(x_i^s)$.

2.2. Seed points auto generation

The 2D scenario, only a few numbers of the seed points are required to be labeled manually to yield a satisfactory segmentation result, while *r* the AR segmentation in this study, it would be tedious and sometimes impractical to specify all the seed points on each slice of the 3D CT volume. Furthermore, employment of applicator type ties closely to specific clinical applications in HDR (figure 2), and the AR (including the applicator and all the packing materials inside the vagina) is not homogenous but contains highly diversified materials such as metal, plastic, air or fluid, etc, which makes the segmentation an extremely challenging task. In this sense, it is meaningful to find a method to minimize user-interaction for seed-points generation for random walks.

Based on a few seed points labeled inside the AR (named *foreground seed points*, or FPs) and outside the AR (named *background seed points*, or BPs) on one slice of the image $\boldsymbol{I}$, in this study, we propose to generate the *incremental foreground point set* (or *i*FPs) and *incremental background point set* (or *i*BPs) for random walks by estimating a probability map. Specifically, let us denote $g^s(s \in \{1, 2\})$ the label representing the foreground (inside of AR) or the background (outside of AR). The intensities of the user-labeled points on a selected slice are denoted as $T = \{t_1, t_2, \ldots, t_c\}$ and their corresponding labels are denoted as $R = \{r_1, r_2, \ldots, r_c\}$, where c is the total number of the user-labeled points. Then, the probability that voxel i in image $\boldsymbol{I}$ belongs to label g^s is estimated by

$$p_i^s = \frac{1}{N^s} \sum_{q, r_q = g^s} \mathrm{e}^{\frac{-(I_i - t_q)^2}{\sigma}}, \tag{4}$$

where σ is a tuning parameter reflecting the rigor level of the similarity criteria, $\boldsymbol{I}_i$ is the intensity of voxel i, and N^s is a normalizing constant for label g^s equal to

$$N^s = \sum_{p=0}^{m} \sum_{q, r_q = g^s} \mathrm{e}^{\frac{-(p-t_q)^2}{\sigma}}, \tag{5}$$

with $m = \max(\boldsymbol{I}_i - \boldsymbol{I}_j), \forall\, i, j$. Thus, the probability of including a new point i to the chain of the FPs can be simply calculated as $p_i = p_i^1/(p_i^1 + p_i^2)$ with 1 representing highest probability.

Then the 3D region growing algorithm is performed on the probability map p_i with the initial user-labeled FPs $\left\{t_1, t_2, \ldots, t_q; r_q = g^1\right\}$ as the seed points and $p_i > p_T$ as the growth condition to obtain the *i*FPs (denoted as $\boldsymbol{F}$). p_T is the threshold to filter those points with high similarity to the user-labeled FPs.

The computation of the *i*BPs is easy and straightforward when the *i*FPs are available. Considering the cylindrical shape of most applicators, we construct a region that resembles a tube to encircle the applicator. Thus, points on the circles centering at the centroid of the *i*FPs on each slice are regarded as the *i*BPs (denoted as $\boldsymbol{B}$). The radii of these circles on each slice are empirically given by 1.5 times the maximum distance of the *i*FPs to the circle center on that slice.

Finally, the random walks algorithm is performed on $\boldsymbol{I}$ using $\boldsymbol{F}$ and $\boldsymbol{B}$ as the FPs and BPs for AR segmentation. The AR is then filled with the CT number of air to yield the image $\boldsymbol{I}'$ (i.e. $\boldsymbol{I}_s'$ and $\boldsymbol{I}_m'$) with an empty *cavity*.

2.3. TPS-RPM for cavity surface point matching

To accommodate large fractional AR deformation, we propose to perform the AR cavity surface point matching using the TPS-RPM algorithm (Chui and Rangarajan 2003, Yang 2011) before DIR in order to minimize registration error. Specifically, given two AR cavity surface point sets $\boldsymbol{X} = \left\{\vec{\boldsymbol{x}}_i = (x_i^x, x_i^y, x_i^z) \;\middle|\; i = 1, 2, \ldots, L\right\}$ from $\boldsymbol{I}_m'$ and $Y = \left\{\vec{\boldsymbol{y}}_j = (y_j^x, y_j^y, y_j^z) \;\middle|\; j = 1, 2, \ldots, N\right\}$ from $\boldsymbol{I}_s'$ in $\mathfrak{R}^3$, the TPS-RPM detects the correspondence between $\boldsymbol{X}$ and $\boldsymbol{Y}$ and match them according to a smooth non-rigid transformation f, which is obtained by minimizing the following objective function:

$$[\widehat{\boldsymbol{P}}, \widehat{f}\,] = \underset{\boldsymbol{P}, f}{\operatorname{argmin}} E(\boldsymbol{P}, f), \tag{6}$$

$$E(\boldsymbol{P}, f) = \sum_{j=1}^{N} \sum_{i=1}^{L} p_{ij} \left\| \vec{\boldsymbol{y}}_j - f(\vec{\boldsymbol{x}}_i) \right\|^2 + \lambda R f^2 + T \sum_{j=1}^{N} \sum_{i=1}^{L} p_{ij} \log p_{ij} - \zeta \sum_{j=1}^{N} \sum_{i=1}^{L} p_{ij}, \tag{7}$$

where λ and ζ are weighting parameters balancing the energy terms in equation (7). R is a smoothness regularization operator, and thin-plate splines (TPS) are applied here. $\boldsymbol{P}$ is a fuzzy correspondence matrix with entries p_{ij} to characterize the correspondence between $\boldsymbol{X}$ and $\boldsymbol{Y}$. T is a temperature parameter for the entropy term $T \sum_{j=1}^{N} \sum_{i=1}^{L} p_{ij} \log p_{ij}$ that is decreased gradually during optimization to enable the fuzzy correspondence matrix to improve gradually and continuously in the space of binary permutation matrices and outliers.

The objective function (6) and (7) are solved in a fashion similar to the expectation-maximization (EM) algorithm involving a dual update process embedded within an annealing scheme: 1) update the correspondence matrix $\boldsymbol{P}$ by fixing the transformation f; and 2) fix $\boldsymbol{P}$ and update the transformation f by minimizing the standard TPS bending energy function. The readers are referred to (Chui and Rangarajan 2003, Yang 2011) for more details regarding the TPS-RPM algorithm. After cavity surface point matching, the transformation f and the corresponding deformed moving cavity surface point set $f(\vec{\boldsymbol{x}}_i)$ are estimated.

2.4. B-spline approximation for initial DVF

Given the original and deformed cavity surface point sets $\vec{\boldsymbol{x}}_i$ and $f(\vec{\boldsymbol{x}}_i)$ on $\boldsymbol{I}_m^{'}$, we would like to approximate a DVF $\boldsymbol{\Delta} = \left\{ \vec{\Delta} = (\Delta^x, \Delta^y, \Delta^z) \;\middle|\; 0 \le x \le \boldsymbol{X}, 0 \le y \le Y, 0 \le z \le Z \right\}$ (or transformation ψ) defined on each voxel of the image as an *initial DVF* for the DIR afterwards. This can be accomplished by estimating a $n_x \times n_y \times n_z$ B-spline control lattice $\boldsymbol{\Phi}$ overlaid on the image domain $\boldsymbol{\Omega} = (x, y, z) \mid 0 \le x \le \boldsymbol{X}, 0 \le y \le Y, 0 \le z \le Z$ with control points $\phi_{i,j,k}$ of uniform spacing d_x, d_y and d_z, in that the transformation ψ can be written as the product of 1D cubic B-spline in terms of the control points (Rueckert *et al* 1999):

$$\vec{\Delta} \equiv \psi(x, y, z) = \sum_{l=0}^{3} \sum_{m=0}^{3} \sum_{n=0}^{3} B_l(u) B_m(\nu) B_n(w) \phi_{i+l, j+m, k+n}, \tag{8}$$

where

$$\begin{aligned} &i = \lfloor x/n_x \rfloor - 1, j = \lfloor y/n_y \rfloor - 1, k = \lfloor z/n_z \rfloor - 1, \\ &u = x/\mathrm{d}_x - \lfloor x/\mathrm{d}_x \rfloor, v = y/\mathrm{d}_y - \lfloor y/\mathrm{d}_y \rfloor, w = z/\mathrm{d}_z - \lfloor z/\mathrm{d}_z \rfloor, \end{aligned} \tag{9}$$

B_l, B_m and B_n are the uniform cubic B-spline basis functions:

$$\begin{aligned} B_0(u) &= (1-u)^3/6, \\ B_1(u) &= (3u^3 - 6u^2 + 4)/6, \\ B_2(u) &= (-3u^3 - 3u^2 + 3u + 1)/6, \\ B_3(u) &= u^3/6. \end{aligned} \tag{10}$$

Let us denote $\delta = \left\{ \vec{\delta}_i = (\delta_i^x, \delta_i^y, \delta_i^z) \;\middle|\; i = 1, 2, \ldots, L \right\}$ the residual differences between $\vec{x}_i$ and $\psi(f(\vec{\boldsymbol{x}}_i))$, it is our objective to approximate a control lattice $\boldsymbol{\Phi}$ that minimizes $\boldsymbol{\delta}$. Consider a subset $\boldsymbol{\delta}'$ of $\boldsymbol{\delta}$ such that each data of $\boldsymbol{\delta}'$ lies in the $4 \times 4 \times 4$ neighborhood of the control point $\phi_{i,j,k}$.

$$\boldsymbol{\delta}' = \left\{ \vec{\delta}' = (\delta^{x_c}, \delta^{y_c}, \delta^{z_c}) \in \boldsymbol{\delta} \;\middle|\; \begin{array}{l} i - 2 \le \lfloor x_c/n_x \rfloor - 1 < i + 2, j - 2 \\ \le \lfloor y_c/n_y \rfloor - 1 < j + 2, k - 2 \le \lfloor z_c/n_z \rfloor - 1 < k + 2 \end{array} \right\}. \tag{11}$$

Assuming that only these neighboring points in $\boldsymbol{\delta}'$ influence the value of $\phi_{i,j,k}$, a least-squared solution to $\phi_{i,j,k}$ which minimizes the approximation error $\boldsymbol{\delta}$ can be simply given by (Hsu *et al* 1992, Lee *et al* 1997):

$$\phi_{i,j,k} = \frac{\sum_c w_c \phi_c}{\sum_c w_c^2}, \tag{12}$$

Algorithm A1:

Initialization

Initialize an uniform B-spline control lattice ϕ_{init} ;

Initialize $\delta = f(\vec{x}_i) - \vec{x}_i$;

Do

1. Estimate the control lattice ϕ' using $\boldsymbol{\delta}$ (equations (12) and (13));
2. Update the control lattice $\phi = \phi_{\text{init}} + \phi'$;
3. Compute ψ (equations (8)) and wrap $f(\vec{x}_i)$ into $\psi(f(\vec{x}_i))$;
4. Update $\boldsymbol{\delta} = \psi(f(\vec{x}_i)) - \vec{x}_i$;

Until $\|\boldsymbol{\delta}_2\| \leq \varepsilon_1$

Obtain Δ **using** $\boldsymbol{\phi}$ (equations(8))

where

$$\begin{aligned}
&\phi_c = \frac{w_c \vec{\delta}'}{\sum_{a=0}^{3}\sum_{b=0}^{3}\sum_{c=0}^{3} w_{abc}},\\
&w_c = w_{lmn} = B_l(v)B_m(u)B_n(w),\\
&l = i + 1 - \lfloor x_c/n_x \rfloor,\ m = j + 1 - \lfloor y_c/n_y \rfloor,\ n = k + 1 - \lfloor z_c/n_z \rfloor,\\
&u = x_c/\mathrm{d}_x - \lfloor x_c/\mathrm{d}_x \rfloor,\ v = y_c/\mathrm{d}_y - \lfloor y_c/\mathrm{d}_y \rfloor,\ w = z_c/\mathrm{d}_z - \lfloor z_c/\mathrm{d}_z \rfloor,
\end{aligned} \tag{13}$$

Note that when $\boldsymbol{\delta}'$ is empty, $\phi_{i,j,k}$ is assigned zero without affecting the approximation error. In practice, $\phi_{i,j,k}$ is estimated in an iterative fashion, so that the transformation ψ is computed using the updated $\phi_{i,j,k}$ to wrap $f(\vec{x}_i)$ into $\psi(f(\vec{x}_i))$ in each iterative step, where the residual difference between $\vec{x}_i$ and $\psi(f(\vec{x}_i))$ is calculated, and the algorithm terminates when the stopping criterion $\|\boldsymbol{\delta}_2\| \leq \varepsilon_1$ (in this work, $\varepsilon_1 = 1.0 \times 10^{-3}$ is empirically adopted to balance accuracy and efficiency) is met. The above B-spline approximation method is summarized in algorithm A1:

2.5. DIR

The moving image $\boldsymbol{I}_m'$ is first deformed with the initial DVF Δ and yield the initial deformed image $\boldsymbol{I}_m'' = \boldsymbol{I}_m' \circ \Delta$, then double force Demons (Wang *et al* 2005, Rogelj and Kovacic 2006, Gu *et al* 2010) is used for the DIR between $\boldsymbol{I}_m''$ and $\boldsymbol{I}_s'$ where the DVF increment du = (dx, dy,dz) is given by

$$\mathbf{du}^{(k+1)} = \frac{(\boldsymbol{I}_m''^{(k)} - \boldsymbol{I}_s')\nabla \boldsymbol{I}_s'}{(\boldsymbol{I}_m''^{(k)} - \boldsymbol{I}_s')^2 + |\nabla \boldsymbol{I}_s'|^2} + \frac{(\boldsymbol{I}_m''^{(k)} - \boldsymbol{I}_s')\nabla \boldsymbol{I}_m''^{(k)}}{(\boldsymbol{I}_m''^{(k)} - \boldsymbol{I}_s')^2 + |\nabla \boldsymbol{I}_m''^{(k)}|^2}, \tag{14}$$

where the superscript k indexes the iteration step. The resulting incremental DVF d$\mathbf{u}$ is smoothed by convolving it with a Gaussian kernel and then added to the global DVF $\mathbf{u}$ to update the moving image. This process is iteratively performed until convergence. The final DVF and deformed moving image is thus obtained by $\Delta + \boldsymbol{u}$ and $\boldsymbol{I}_m' \circ (\Delta + \mathbf{u})$, respectively.

2.6. Implementation

In this section, we will present a few practical issues pertaining to the algorithm implementation.

As described in section 2.1, the Laplacian matrix L is a highly sparse matrix, to facilitate solving the sparse linear system, we adopt the CUSP (Dalton and Bell 2012), a CUDA-based library for sparse linear algebra and graph computations, to solve the sparse linear equation (3). The sparse matrices are stored using the coordinate (COO) format, and the conjugate gradient (CG) method is used as the iterative solver with relative tolerance of 10^{-6} and maximum iteration 1000 as the stopping criteria. The parameter $\beta = 90$ is empirically chosen.

For seed-points auto-generation, we set the tuning parameter $\sigma = 0.2\,\mathrm{m}$, where $m = \max(\boldsymbol{I}_i - \boldsymbol{I}_j), \forall\, i, j$ (equations (4) and (5)) to keep the choice of σ relevant to images of different intensity and contrast levels. A relatively rigorous threshold $p_T = 0.9$ is used as the growing condition of the FPs in this study. Hence, only those points with high similarity to the user-labeled FPs will be grown and included into the chain of the FPs.

A multi-scale strategy is also adopted in Demons to reduce the magnitude of the displacement vectors with respect to the voxel size and hence avoid the local minima problem in registration to a certain extent (Gu *et al* 2010). The iteration starts with the lowest resolution images, and at the end of each level, the moving vectors are up-sampled to serve as the initial solution at the finer level. In this work, we consider two different resolution levels. Further down-sampling was found to be unnecessary to improve registration accuracy or efficiency. For the stopping criteria regarding whether the moving image has been correctly deformed, we use a convergence criterion based on the difference between successive deformation fields. We define a relative norm $l^{(k)} = \sum |\mathrm{d}\mathbf{u}^{(k+1)}| / \sum |\mathbf{u}^{(k)}|$, and use $l^{(k-10)} - l^{(k)} \leq \varepsilon_2$, where $\varepsilon_2 = 1.0 \times 10^{-4}$, as our stopping criterion. This measure is found to have a close correspondence with accuracy, as DIR is stopped when there is no 'force' to push voxels any more (Gu *et al* 2010).

In this work, the initial seed point labelling and seed-points auto-generation are implemented in Matlab (Mathworks, Inc.) with a graphical user interface (GUI) to facilitate user interaction, while the random walks segmentation, the TPS-RPM point matching, the B-spline DVF approximation and the Demons-based DIR in SPEED are implemented under the compute unified device architecture (CUDA) programming environment and GPU hardware platform to yield a satisfactory efficiency. Main data parallel GPU kernels coded in SPEED include: kernels in the random walks segmentation: 1) an edge kernel to build a graph with vertices and edges, 2) a weighting kernel to compute and normalize ω_{ij}, and 3) a Laplacian kernel to create the Laplacian sparse matrix; kernels in the TPS-RPM point matching: 1) an update kernel for calculation of the correspondence matrix $\boldsymbol{P}$, 2) an update kernel for the TPS transformation parameters estimation, and 3) a transformation kernel to deform the moving points; kernels in the B-spline DVF approximation: 1) a grid fitting kernel to approximate and update the B-spline control lattice, and 2) a transformation kernel to wrap points by the B-spline control lattice; kernels in the Demons DIR: 1) a Gaussian filter kernel to smooth images and moving vectors; 2) a gradient kernel to calculate the gradient of images; 3) a moving vector kernel to calculate and update moving vectors; 4) an interpolation kernel to deform images with moving vectors; 5) a comparison kernel to stop the program based on the stopping criteria.

Considering all the components mentioned above, we summarize the SPEED algorithm in algorithm A2.

2.7. Quantification of segmentation and DIR

The effectiveness of SPEED is quantitatively evaluated by measuring both the performance of the segmentation and the DIR. The segmentation accuracy is assessed by Dice ratio and percent error. Given the ground truth region A and the segmented region B, the Dice ratio is

Algorithm A2:

A. AR removal

1. Initial seed point labelling and probability map estimations (equations (4) and (5)) on $\boldsymbol{I}_s$ and $\boldsymbol{I}_m$, respectively;
2. Obtain *i*FPs on $\boldsymbol{I}_s$ and $\boldsymbol{I}_m$ by region growing on the corresponding probability maps, and yield *i*BPs by encircling *i*FPs;
3. Solve the random walks equation (equations (3)) to obtain the AR-free images $\boldsymbol{I}_s^{'}$ and $\boldsymbol{I}_m^{'}$.

B. Cavity surface point matching

1. Extract the two AR cavity surface point sets $\vec{\boldsymbol{x}}_j$ and $\vec{\boldsymbol{y}}_j$ from the corresponding AR segmentations on $\boldsymbol{I}_m^{'}$ and $\boldsymbol{I}_s^{'}$;
2. Obtain $f(\vec{\boldsymbol{x}}_i)$ by performing the TPS-RPM point matching between $\vec{\boldsymbol{x}}_j$ and $\vec{\boldsymbol{y}}_j$ (equations (6)–(7)).

C. Initial DVF approximation by B-spline

Obtain the initial DVF Δ by performing Algorithm A1

D. DIR

1. Initially deform $\boldsymbol{I}_m^{'}$ by $\boldsymbol{I}_m^{''} = \boldsymbol{I}_m^{'} \circ \Delta$;
2. Calculate DVF $\mathbf{u}$ by performing Demons DIR between $\boldsymbol{I}_m^{''}$ and $\boldsymbol{I}_s^{'}$ (equations (14));
3. Obtain the final DVF $\Delta + \mathbf{u}$ and deformed moving image $\boldsymbol{I}_m^{'} \circ (\Delta + \mathbf{u})$

defined as $2 \times |A \bigcap B|/(|A| + |B|)$, and it ranges from 0 ~ 1, corresponding to the worst and the best agreement of the two regions. Generally, 0.7 is considered as satisfactory segmentation (Zijdenbos *et al* 1994, Shi *et al* 2009). The percent error is defined as $(A \bigcup B - A \bigcap B)/A$ with 0 representing the best segmentation. The ground truth segmentations are contoured by an experienced physician.

DIR performance is measured by three similarity metrics. The first metric is the structural similarity (SSIM) index (Zhou *et al* 2004), which tries to measure similarity between two images based on extracted structural information. The second metric is the normalized mutual information (NMI). Both SSIM and NMI range in [0, 1] with 1 representing the most image similarity. The third metric is the root mean squared error (RMSE) between two edge images:

$$\mathrm{RMSE}_{\mathrm{edge}} = \sqrt{\sum_{i}^{N} (\boldsymbol{I}_1^{\mathrm{edge}}(i) - \boldsymbol{I}_2^{\mathrm{edge}}(i))^2 / N}, \tag{15}$$

where $\boldsymbol{I}_1^{\mathrm{edge}}(i)$ and $\boldsymbol{I}_2^{\mathrm{edge}}(i)$ are the binary Canny edge images of image $\boldsymbol{I}_1$ and $\boldsymbol{I}_2$, respectively (Canny 1986), N is the number of voxels in images $\boldsymbol{I}_1$ or $\boldsymbol{I}_2$. When two images are perfectly registered, $\mathrm{RMSE}_{\mathrm{edge}}$ should be zero. These three similarity metrics serve as quantitative evaluation tools in addition to the visual inspection of the registration results, namely comparing the deformed CT image and the static CT image in two different HDR fractions.

2.8. Synthetic data

To validate our algorithm, we have simulated a test dataset with realistic fractional deformation based on a HDR CT image (denoted as $\mathrm{CT}_{\mathrm{sim}}^{f1}$) from a gynecologic cancer patient. Firstly, a known rigid transformation (denoted as $\mathrm{DVF}_{\mathrm{sim}}^{\mathrm{rigid}}$) is applied on $\mathrm{CT}_{\mathrm{sim}}^{f1}$ to yield a rigidly transformed HDR CT image (denoted as $\mathrm{CT}_{\mathrm{Sim}}^{\mathrm{rigid}}$). Then, a deformable B-spline transformation

(denoted as $\mathrm{DVF}_{\mathrm{sim}}^{\mathrm{deform}}$) to simulate tissue deformation in $\mathrm{CT}_{\mathrm{Sim}}^{\mathrm{rigid}}$ is generated by changing the B-spline control lattice overlaid on $\mathrm{CT}_{\mathrm{Sim}}^{\mathrm{rigid}}$ through manually dragging several B-spline control lattice points located away from the AR. By doing this, only the tissue regions are subjected to deformation, while deformation inside the AR is negligible. Finally, the combined transformation $\mathrm{CT}_{\mathrm{Sim}}^{\mathrm{rigid}}+\mathrm{DVF}_{\mathrm{sim}}^{\mathrm{deform}}$ (denoted as $\mathrm{DVF}_{\mathrm{sim}}^{\mathrm{gt}}$) is used to wrap $\mathrm{CT}_{\mathrm{sim}}^{f1}$ and yield a deformed HDR CT image (denoted as $\mathrm{CT}_{\mathrm{sim}}^{f2}$). Note that $\mathrm{DVF}_{\mathrm{sim}}^{\mathrm{gt}}$ resembles realistic deformation between HDR fractions because it mimics rigid and deformable transformations in the tissues but only rigid transformations in AR. This approach offers us the ground truth for the evaluation of SPEED: $\mathrm{CT}_{\mathrm{sim}}^{f1}$ and $\mathrm{CT}_{\mathrm{sim}}^{f2}$ can be regarded as the moving and static CT images from two HDR fractions, respectively, and $\mathrm{DVF}_{\mathrm{sim}}^{\mathrm{gt}}$ is the ground truth DVF used to compare with that calculated by SPEED (denoted as $\mathrm{DVF}_{\mathrm{sim}}^{\mathrm{SPEED}}$).

2.9. Clinical data

We use CT images of nine clinical HDR cases from three gynecologic cancer patients (three HDR fractions per patient, termed as fx1, fx2, fx3 in the following text) to test SPEED. These cases involve a scenario of utilization of two types of applicators, i.e. tandem and ovoids (T and O) applicator and tandem and cylinder (T and C) applicator. Patient 1 uses different types of application in different fractions and patient 2 and 3 use the same type of applicator (T and O applicator). The resolution of all the CT images in the transverse plane is 512 × 512 with pixel spacing of 0.98 mm, and the slice thickness is 2.5 mm. For each patient, fx1 is used as the static fraction, while fx2 and fx3 are used as the moving fraction in this study. Thus, the CT images in fx2 and fx3 are cropped and re-sampled to match the dimension and resolution of that in fx1 after rigid registration, and all CT images are then down-sampled to half of their original size in the transverse plane. Hence, the sizes of images after rigid registration are 256 × 256 × 54 (Case 1, 2, 3), 256 × 256 × 50 (Case 4, 5, 6) and 256 × 256 × 52 (Case 7, 8, 9) for patient 1, 2 and 3, respectively, and the voxel size is 1.96 × 1.96 × 2.5 mm for all the CT images.

For clarity, the following symbols are used to represent different images used in the algorithm evaluation: $\mathrm{CT}_{\mathrm{App}}^{f1}$, $\mathrm{CT}_{\mathrm{App}}^{f2}$ and $\mathrm{CT}_{\mathrm{App}}^{f3}$ are the HDR CT images with applicator before DIR in fx1, fx2 and fx3, respectively. $\mathrm{dCT}_{\mathrm{App}}^{f2\rightarrow f1}$ and $\mathrm{dCT}_{\mathrm{App}}^{f3\rightarrow f1}$ are the deformed $\mathrm{CT}_{\mathrm{App}}^{f2}$ and $\mathrm{CT}_{\mathrm{App}}^{f3}$ images to match $\mathrm{CT}_{\mathrm{App}}^{f1}$ after DIR, and the corresponding DVF are $\mathrm{DVF}_{\mathrm{App}}^{f2\rightarrow f1}$ and $\mathrm{DVF}_{\mathrm{App}}^{f3\rightarrow f1}$, respectively. Similarly, $\mathrm{CT}_{\mathrm{NoApp}}^{f1}$, $\mathrm{CT}_{\mathrm{NoApp}}^{f2}$ and $\mathrm{CT}_{\mathrm{NoApp}}^{f3}$ are the HDR CT images with AR removed before DIR in fx1, fx2 and fx3, respectively. $\mathrm{dCT}_{\mathrm{NoApp}}^{f2\rightarrow f1}$ and $\mathrm{dCT}_{\mathrm{NoApp}}^{f3\rightarrow f1}$ are the deformed $\mathrm{CT}_{\mathrm{NoApp}}^{f2}$ and $\mathrm{CT}_{\mathrm{NoApp}}^{f3}$ images to match $\mathrm{CT}_{\mathrm{NoApp}}^{f1}$ after DIR, and the corresponding DVFs are $\mathrm{DVF}_{\mathrm{NoApp}}^{f2\rightarrow f1}$ and $\mathrm{DVF}_{\mathrm{NoApp}}^{f3\rightarrow f1}$, respectively. SP^{f1}, SP^{f2}, and SP^{f3} are the AR cavity surface points in $\mathrm{CT}_{\mathrm{App}}^{f1}$, $\mathrm{CT}_{\mathrm{App}}^{f2}$ and $\mathrm{CT}_{\mathrm{App}}^{f3}$, respectively. $\mathrm{dSP}^{f2\rightarrow f1}$ and $\mathrm{dSP}^{f3\rightarrow f1}$ are the deformed SP^{f2} and SP^{f3} to match SP^{f1} by the TPS-RPM algorithm, and $\mathrm{DVF}_{\mathrm{init}}^{f2\rightarrow f1}$ and $\mathrm{DVF}_{\mathrm{init}}^{f3\rightarrow f1}$ the corresponding initial DVF approximated by B-spline, respectively.

3. Results

3.1. Impact of AR removal on DIR

It is interesting to know whether the existence of the AR would influence the DIR accuracy in those tissues surrounding AR. To evaluate this, we first compare the DIR results with and without AR removal using the Demons algorithm. Figure 3 shows an exemplary comparison

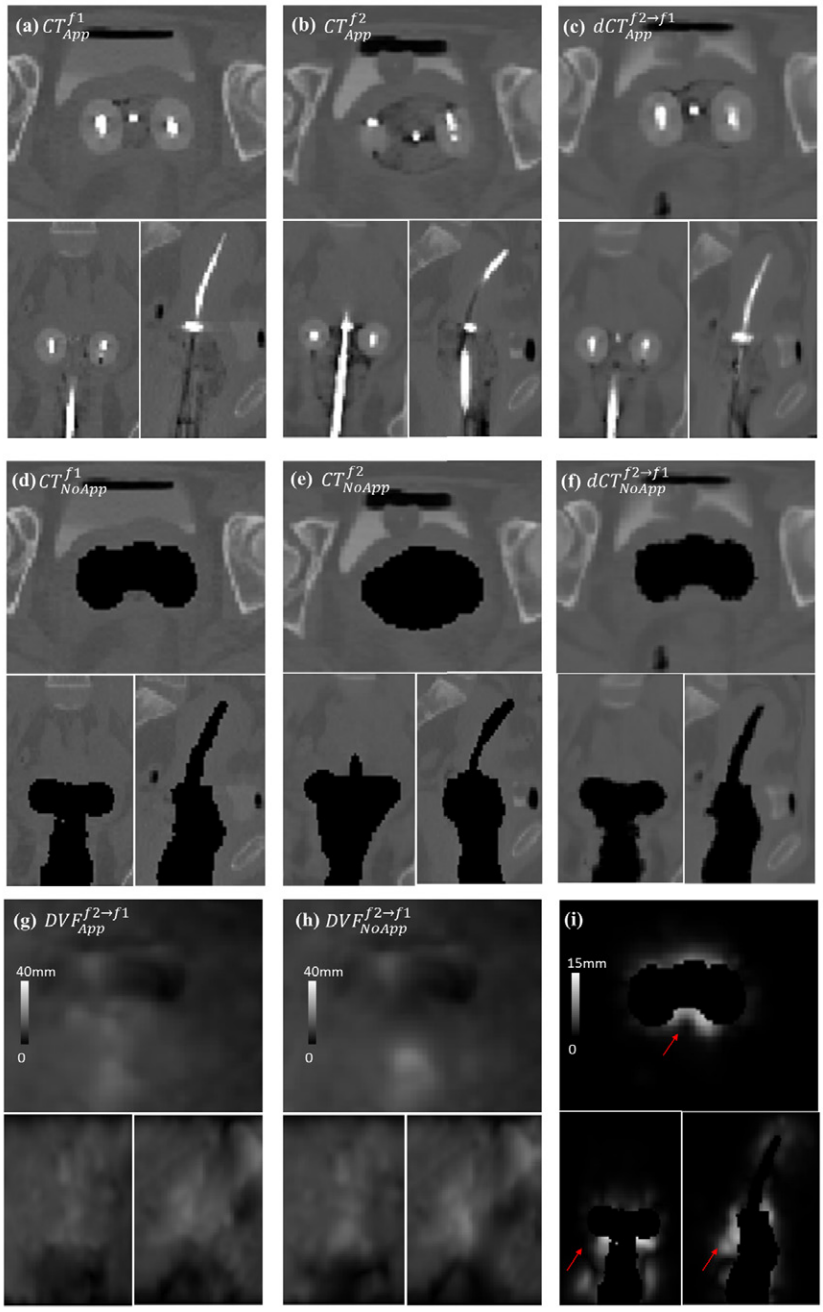

Figure 3. DVF comparison of DIR with and without AR removal (Case 4, 5). (*a*) CT_{App}^{f1}; (*b*) CT_{App}^{f2}; (*c*) $dCT_{App}^{f2\to f1}$ by Demons; (*d*) CT_{NoApp}^{f1}; (*e*) CT_{NoApp}^{f2}; (*f*) $dCT_{NoApp}^{f2\to f1}$ by Demons; (*g*) $DVF_{App}^{f2\to f1}$; (*h*) $DVF_{NoApp}^{f2\to f1}$; (*i*) Difference image between $DVF_{App}^{f2\to f1}$ and $DVF_{NoApp}^{f2\to f1}$ in regions outside of the AR. The red arrows indicate the large DVF differences. The ARs are manually contoured and removed by an experienced physician.

Table 1. Mean and maximum DVF differences in regions outside the AR between DIR with and without AR removal for patient 1 ~ 3.

		fx2 → fx1(mm)	fx3 → fx1(mm)
Patient 1	Mean(STD)	2.3 (±1.2)	2.5 (±1.5)
	Maximum	9.1	12.3
Patient 2	Mean(STD)	2.6 (±2.1)	3.0(±2.9)
	Maximum	12.7	22. 8
Patient 3	Mean(STD)	3.4(±3.1)	2.2 (±1.4)
	Maximum	19.1	10.3

of DIR with and without AR removal using fractional HDR CT images (Case 4, 5) from patient 2. The ARs in evaluated HDR CT images are manually contoured and removed by an experienced physician. Visually inspecting the deformed CT images (figures 3(*c*) and (*f*)) with the static CT images (figures 3(*a*) and (*d*)), good alignments are obtained in both scenarios. However, if we compare the corresponding DVF (figures 3(*g*) and (*h*)) instead, large DVF differences are observed outside of the AR (figure 3(*i*)). These DVF differences are essentially caused by the DVF propagation from the AR to its surrounding tissues.

Table 1 shows the results of the mean and maximum DVF differences in regions outside the AR (i.e. the patient volume exclusive of the AR), between DIR with and without AR removal for patient 1 ~ 3. We can see that the mean DVF differences range from 2.2 to 3.4 mm and the maximum DVF differences range from 9.1 to 22.8 mm, implying that significant DIR errors will occur if the applicator is onsite. This point can be further elaborated by examining the histograms of the DVF differences, which are shown in figure 4. For all the cases, we can observe that although the affected volume drops gradually as the DVF difference increases, yet, considerably large volumes are subject to DVF difference, especially when the DVF difference is <5 mm. In other words, DIR errors are distributed vastly instead of locally in regions surrounding the AR and large amount of adjacent soft tissues suffer from such DIR errors, which are less likely to be ignored because these affected volumes are essentially high dose regions. It is the influence of AR on DIR shown above that prompts us to segment and remove the AR in the HDR CT images before performing DIR.

3.2. AR segmentation

We present the AR segmentation results in figure 5. Figure 5(*a*) illustrates an example of the seed-points generation in Case 4. A few FPs and BPs are firstly labeled on one axial slice of the CT image (figure 5(*a*)-1), and the corresponding *i*FPs and *i*BPs (figure 5(*a*)-2) to feed the random walks segmentation are then calculated by the seed-points generation scheme which was detailed in section 2.2. The corresponding segmentation result is shown in figure 5(*a*)-3. Figure 5(*b*) summarizes the AR segmentation results for the other eight cases. We can observe that, for all the evaluated cases, the ARs shaped by different types of applicators and different inhomogeneous packing materials are all successfully segmented. The segmentation results are also quantitatively compared with the ground truths contoured by an experienced physician using two metrics, i.e. the Dice ratio and percent error, which are listed in table 2. The mean Dice ratio and percent error of the 9 cases are 0.9(±0.02) and 0.2(±0.04), respectively, indicating outstanding segmentation performance.

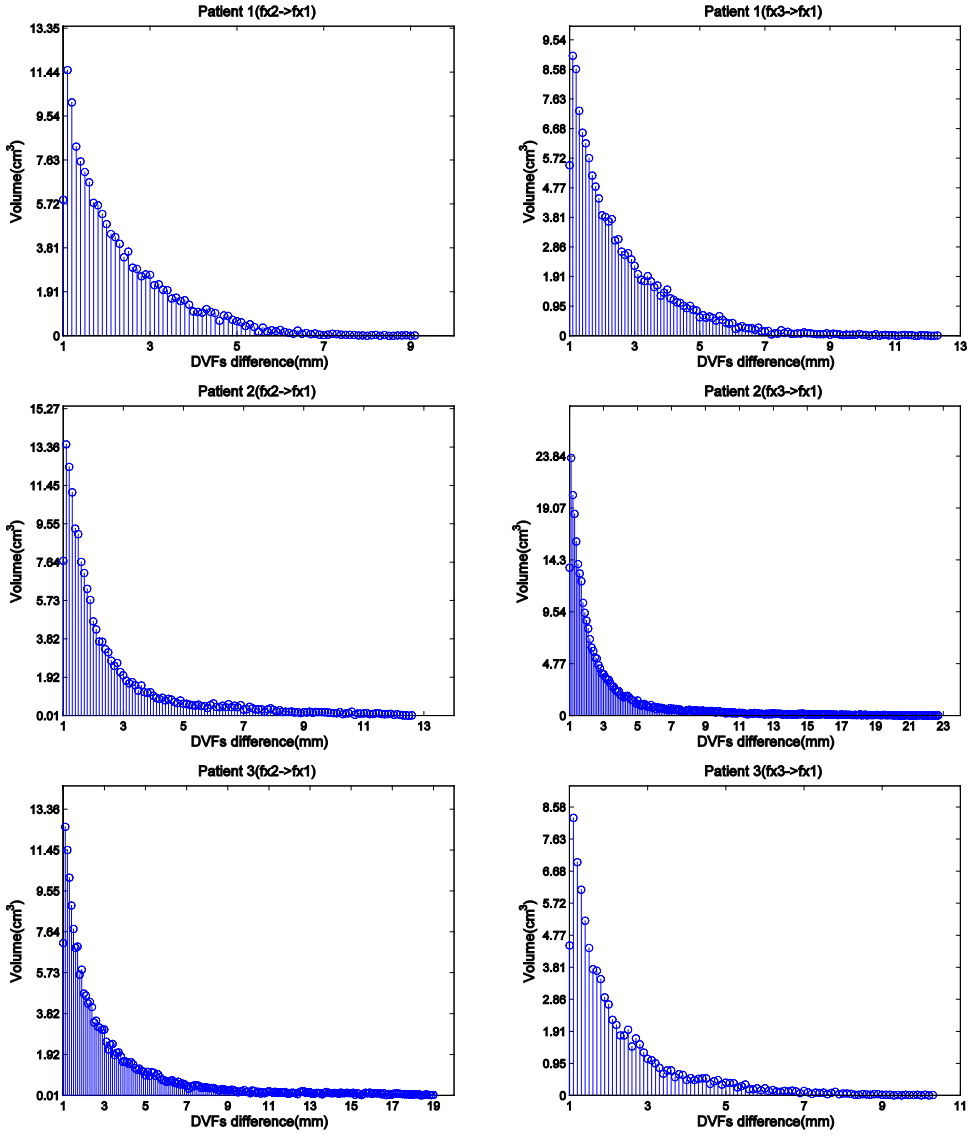

Figure 4. Histograms of the DVF difference (>1 mm) in regions outside the AR between DIR with and without AR removal for patient 1~3.

3.3. DIR results: synthetic data

Figure 6 shows the DIR results for the synthetic case. Figure 6(*a*) is a HDR CT image $\mathrm{CT}_{\mathrm{sim}}^{f1}$ overlaid with a known rigid transformation $\mathrm{DVF}_{\mathrm{sim}}^{\mathrm{rigid}}$, and the rigidly transformed image $\mathrm{CT}_{\mathrm{Sim}}^{\mathrm{rigid}}$ is shown in figure 6(*b*). A deformable B-spline transformation $\mathrm{DVF}_{\mathrm{sim}}^{\mathrm{deform}}$ is simulated using the approach described in section 2.7 and overlaid on $\mathrm{CT}_{\mathrm{Sim}}^{\mathrm{rigid}}$ (figure 6(*b*)). We can see that the $\mathrm{DVF}_{\mathrm{sim}}^{\mathrm{deform}}$ arises mainly from the soft tissue region, in contrast, the AR has negligible deformable transformation. The combined transformation $\mathrm{DVF}_{\mathrm{sim}}^{\mathrm{gt}}$ is applied on $\mathrm{CT}_{\mathrm{sim}}^{f1}$ to yield $\mathrm{CT}_{\mathrm{sim}}^{f2}$ (figure 6(*c*)). The $\mathrm{DVF}_{\mathrm{sim}}^{\mathrm{gt}}$, which is also shown as a grayscale image in figure 6(*d*), can be

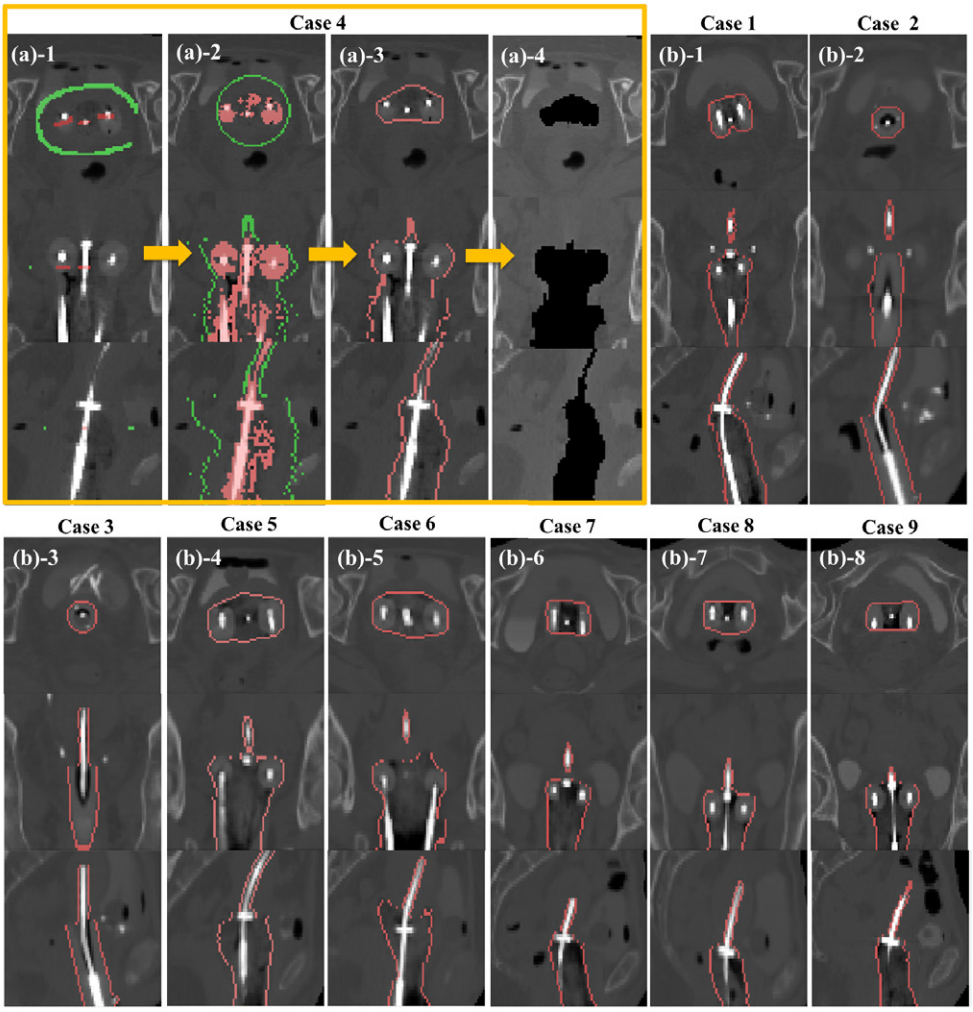

Figure 5. Illustration of seed points labelling, *i*FPs/*i*BPs auto-generation, AR segmentation and removal in Case 4 (*a*) and AR segmentation results of other eight cases (*b*). (*a*)-1. FPs (red) and BPs (green) labeled on one axial slice; (*a*)-2. Auto-generated *i*FPs (red) and *i*BPs (green); (*a*)-3. AR segmentation result (red curve); (*a*)-4. AR removed; (*b*)-1 ~ 8: AR segmentation results (red curves) of the other eight cases. The three rows are axial, coronal and sagittal views, respectively.

Table 2. The Dice ratio (DR) and percent error (PE) of the AR segmentation of the nine cases.

	Patient1			Patient 2			Patient 3		
	Case1	Case 2	Case 3	Case 4	Case 5	Case 6	Case 7	Case 8	Case 9
DR	0.87	0.90	0.86	0.89	0.90	0.92	0.92	0.91	0.92
PE	0.25	0.21	0.27	0.22	0.20	0.15	0.16	0.18	0.15

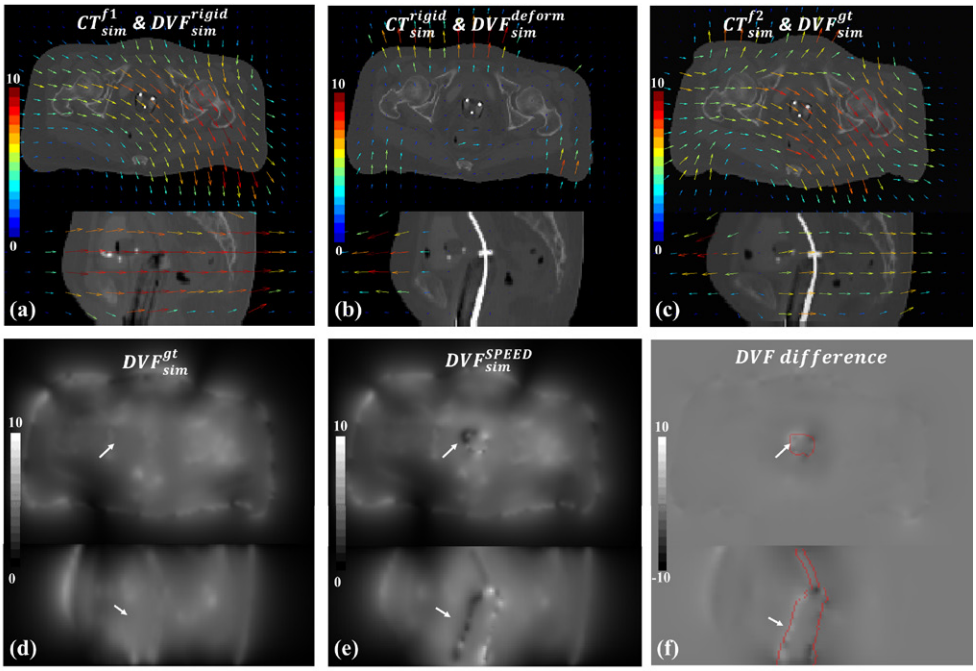

Figure 6. Synthetic data and DIR results (display DVF unit is 'voxels'): (*a*): DVF^{rigid}_{sim} overlaid on CT^{f1}_{sim}; (*b*) DVF^{deform}_{sim} overlaid on CT^{rigid}_{Sim}; (*c*) DVF^{gt}_{sim} overlaid on CT^{f2}_{sim} (*d*) DVF^{gt}_{sim}; (*e*) DVF^{SPEED}_{sim}; (*f*) DVF difference. The first and second rows in each subfigure are the axial and sagittal views, respectively. The red contour in (*f*) indicates the AR region, and the arrows in (*d*) ~ (*f*) indicate DVF difference of the AR region.

regarded as the ground truth DVF between CT^{f1}_{sim} and CT^{f2}_{sim}. DIR is then performed between CT^{f1}_{sim} and CT^{f2}_{sim} using SPEED, and the calculated DVF DVF^{SPEED}_{sim} is shown in figure 6(*e*). We can see that the SPEED algorithm can produce almost the same DVF as the ground truth (figure 6(*f*)), and the major DVF differences are located inside the AR (arrows in figure 6(*d*)–(*f*)). It is found that the mean and standard deviation of the DVF differences inside and outside of the AR are −0.77(±1.28) and −0.07(±0.32) voxels, respectively. The existence of relatively large DVF difference inside AR is legitimate because unlike the ground truth DVF^{gt}_{sim}, the DVFs of DVF^{SPEED}_{sim} inside the AR embrace little mapping information but merely undesirable DVF propagated from neighboring tissues since the AR is segmented and removed in SPEED.

3.4. DIR results: clinical data

In terms of DIR accuracy, the proposed method is quantitatively evaluated using SSIM, NMI and Canny edge RMSE between $dCT^{f2\rightarrow f1}_{NoApp}$ and CT^{f1}_{NoApp}, and $dCT^{f3\rightarrow f1}_{NoApp}$ and CT^{f1}_{NoApp}, where $dCT^{f2\rightarrow f1}_{NoApp}$ and $dCT^{f3\rightarrow f1}_{NoApp}$ are obtained using the Demons or SPEED. A region of interest (ROI) with axial size of 50 × 50 centering at the AR on each CT image is extracted for similarity assessment, and the quantitative results are detailed in table 3. Both Demons and SPEED increase SSIM and NMI, as well as reduce Canny edge RMSE after DIR. The average SSIM increases from 0.15 ± 0.06 to 0.46 ± 0.17 and 0.54 ± 0.08 after DIR by Demons and SPEED, respectively. The average NMI increases from 0.53 ± 0.01 to 0.56 ± 0.01 and 0.57 ± 0.01

Table 3. SSIM, NMI and Canny edge RMSE of the ROI centering at AR between $dCT^{f2\rightarrow f1}_{NoApp}$ and CT^{f1}_{NoApp}, $dCT^{f3\rightarrow f1}_{NoApp}$ and CT^{f1}_{NoApp}.

		SSIM		NMI		Canny Edge RMSE	
		fx2 → fx1	fx3 → fx1	fx2 → fx1	fx3 → fx1	fx2 → fx1	fx3 → fx1
Patient1	Before DIR	0.06 (±0.04)	0.20 (±0.11)	0.52	0.54	0.36	0.33
	Demons	0.35 (±0.16)	0.53 (±0.16)	0.55	0.57	0.31	0.26
	SPEED	0.45 (±0.09)	0.57 (±0.12)	0.56	0.57	0.29	0.25
Patient 2	Before DIR	0.22 (±0.08)	0.14 (±0.08)	0.53	0.53	0.33	0.34
	Demons	0.55 (±0.14)	0.49 (±0.08)	0.56	0.56	0.28	0.28
	SPEED	0.59 (±0.17)	0.56 (±0.06)	0.57	0.56	0.25	0.26
Patient 3	Before DIR	0.17 (±0.09)	0.11 (±0.08)	0.53	0.53	0.36	0.36
	Demons	0.48 (±0.20)	0.37 (±0.29)	0.56	0.55	0.33	0.32
	SPEED	0.64 (±0.16)	0.43 (±0.29)	0.59	0.55	0.28	0.31

after DIR by Demons and SPEED, respectively. The average canny edge RMSE decreases from 0.34 ± 0.02 to 0.30 ± 0.03 and 0.27 ± 0.02 after DIR by Demons and SPEED, respectively. These results show that SPEED behaves better than Demons for all the three metrics.

The improvement of SPEED over Demons can be further examined by visual inspection of the DIR results with different applicator types in figure 7 (T and O and T and C applicators) and with the same applicator type in figure 8 (both T and O applicators). We can see that, regions around the tandem tip of the applicator fail to be aligned via Demons-based DIR between the two AR-free HDR CT images, and this misalignment is observed in both scenarios when different (figure 7(*k*)) or same type (figure 8(*k*)) of applicators are inserted in different HDR fractions. By applying SPEED, the approximated initial DVF obtained by registering the two AR cavity surface points using TPS-RPM can provide a favorable initial match (figures 7(*g*)–(*i*), figures 8(*g*)–(*i*)), which serves as a good starting point for the Demons afterward, and therefore, more accurate DIR results can be expected, especially in tissues neighboring the AR (figures 7(*l*) and 8(*l*)). This is critical because dose is relatively higher on the AR surface than in regions far from the AR center, and it is this fact that the DIR accuracy on AR surface is of great significance in HDR dose mapping. Similar observations are also made in other patients, thus we do not repeat the results.

3.5. Impact of segmentation accuracy

To quantify the segmentation induced registration error, we compare the DIR results generated by SPEED using the ground truth manual segmentation and that computed by the proposed random walks-based segmentation scheme in this work. Specifically, the physician delineated AR and the computed AR are first obtained, and then serve as inputs for the sequential TPS-RPM point matching, initial DVF approximation, and Demons DIR steps in SPEED. Then,

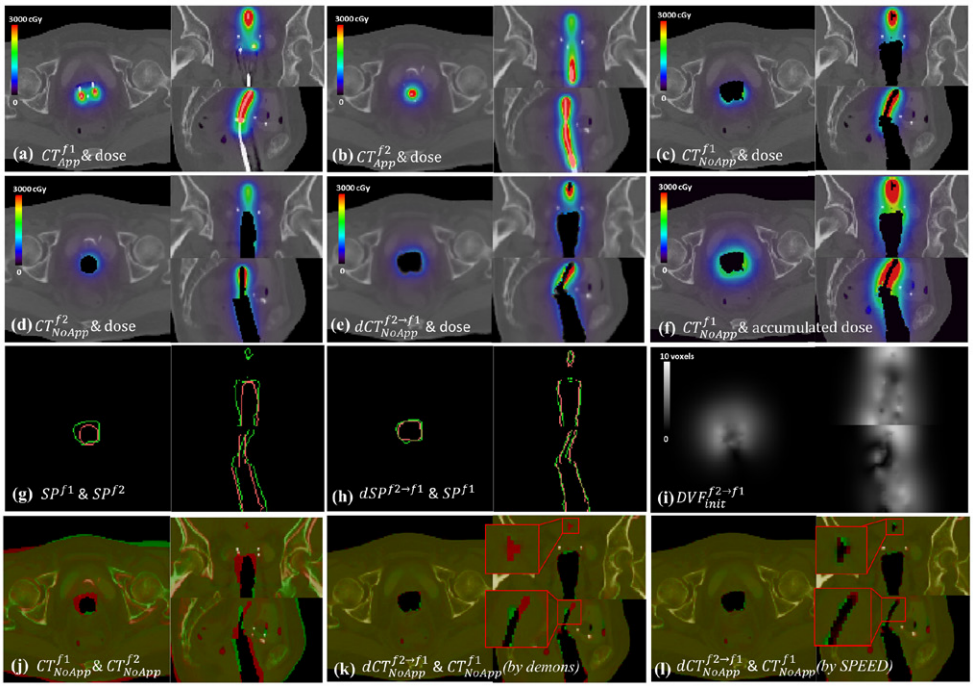

Figure 7. DIR results of HDR CT images with T and O applicator (Case1, i.e. fx1 of patient 1) and T and C applicator (Case 2, i.e. fx2 of patient 1). (*a*) $\mathrm{CT}_{\mathrm{App}}^{f1}$ overlaid with dose; (*b*) $\mathrm{CT}_{\mathrm{App}}^{f2}$ overlaid with dose; (*c*) $\mathrm{CT}_{\mathrm{NoApp}}^{f1}$ overlaid with dose; (*d*) $\mathrm{CT}_{\mathrm{NoApp}}^{f2}$ overlaid with dose; (*e*) $\mathrm{dCT}_{\mathrm{NoApp}}^{f2\rightarrow f1}$ overlaid with deformed dose; (*f*) $\mathrm{CT}_{\mathrm{NoApp}}^{f1}$ overlaid with accumulated dose; (*g*) SP^{f1} (green) and SP^{f2} (red); (*h*) SP^{f1} (green) and $\mathrm{dSP}^{f2\rightarrow f1}$ (red); (*i*) $\mathrm{DVF}_{\mathrm{init}}^{f2\rightarrow f1}$; (*j*) $\mathrm{CT}_{\mathrm{NoApp}}^{f1}$ (green) and $\mathrm{CT}_{\mathrm{NoApp}}^{f2}$ (red); (*k*) $\mathrm{dCT}_{\mathrm{NoApp}}^{f2\rightarrow f1}$ (red) by Demons and $\mathrm{CT}_{\mathrm{NoApp}}^{f1}$ (green); (*l*) $dCT_{\mathrm{NoApp}}^{f2\rightarrow f1}$ (red) by SPEED and $\mathrm{CT}_{\mathrm{NoApp}}^{f1}$ (green).

the final DVFs as well as the deformed CT images generated using these two AR sets by SPEED can be utilized for DIR discrepancy analysis. Figure 9 shows the DVFs differences and the similarity indices between the deformed CT images using the calculated and ground truth segmentation in SPEED. The inaccuracy of the AR segmentation is quantified by the percent error, which is defined previously in section 2.6. The average percent error between the calculated and ground truth segmentation of two fractional CT images ranges from 15 to 26%, and such segmentation errors induce mean DVFs differences around of the AR ranging from 0.1 ± 0.5 to 0.2 ± 0.7 mm. The mean DVFs difference for all the evaluated cases is 0.1 ± 0.5 mm, and the mean Canny edge RMSE, NMI and SSIM between the deformed CT images are 0.08, 0.86, 0.99 ± 0.004, respectively. The statistics suggest that the proposed segmentation scheme is accurate and robust for AR segmentation and small proportion of inaccurate AR segmentation causes only minor and acceptable registration errors.

3.6. Efficiency

All the experiments in this study were conducted on a GPU platform with an NVIDIA Telsa C2075 card with a total number of 448 processors of 1.15 GHz. It is also equipped with 6 GB GDDR5 memory, shared by all processors. The computational times of the main procedures,

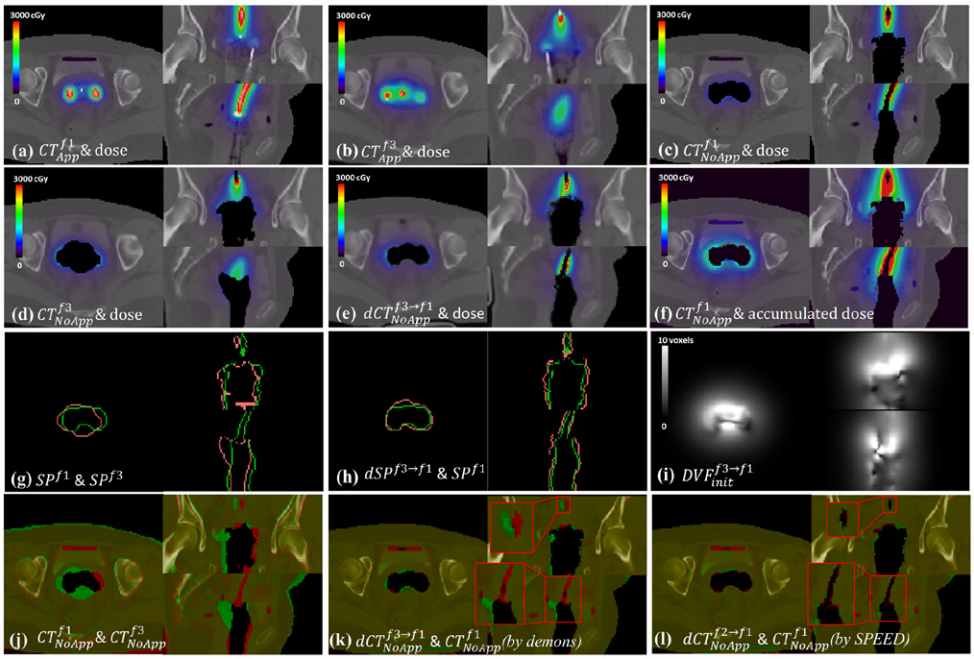

Figure 8. DIR results of two HDR CT images with both T and O applicators (Case 4 and 6, i.e. fx1 and fx3 of patient 2). (*a*) ~ (*l*) have the same arrangements with those in figure 7.

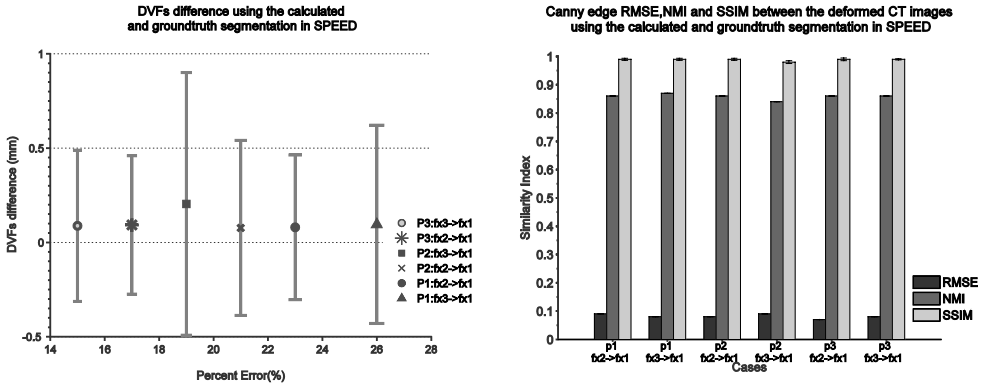

Figure 9. Error bar of the DVFs differences around of the AR (left) and the similarity indices between the deformed CT images (right) using the calculated and ground truth segmentation in SPEED. In the left figure, markers and both ends in each case indicate the mean and standard deviation of the DVFs differences, respectively, and the *x* axis is the average percent error between the calculated and ground truth segmentation of two fractional CT images.

i.e. AR removal, TPS-RPM point matching, B-spline DVF approximation and Demons DIR, in SPEED are listed in table 4. It can be seen that the computational time depends on the complexity of the cases tested. Currently, for the typical clinical patient cases shown here, the runtime is about 1 ~ 1.5 min.

Table 4. Computational times of the main procedures in SPEED for patients 1–3.

		Time (sec)				
		AR removal	TPS-RPM point	B-spline DVF	Demons	
		(fx2,fx3\fx1)	matching	approximation	DIR	Total
Patient 1	fx2 → fx1	24.0\25.3	23.5	0.4	7.4	80.6
	fx3 → fx1	23.8\25.3	29.1	0.37	8.1	86.7
Patient 2	fx2 → fx1	28.6\28.8	27.6	0.37	7.5	92.9
	fx3 → fx1	28.4\28.8	32.9	0.37	9.3	99.8
Patient 3	fx2 → fx1	23.6\23.3	9.46	0.37	8.1	64.8
	fx3 → fx1	22.8\23.3	9.89	0.37	8.1	64.5

4. Discussion and conclusions

In this paper, we have successfully applied a novel DIR scheme that incorporates a segmentation step and a point matching step, namely SPEED, to the challenging DIR problem of HDR CT images with inserted applicator for gynecological cancer patients. Though hitherto many methods had been proposed and studied to address different DIR issues in radiotherapy (Gao *et al* 2006, Godley *et al* 2009, Paquin *et al* 2009, Xie *et al* 2009, Yang *et al* 2009, Nithiananthan *et al* 2012, Zhen *et al* 2012, Gu *et al* 2013, Huger *et al* 2013, Kim *et al* 2013, Pace *et al* 2013, Zhen *et al* 2013), yet, none of these methods are suitable for the registration problem of the HDR CT images with inserted medical apparatus, such as vaginal applicators and radiation source. Therefore, it is appealing to develop a more accurate DIR method to handle the DIR between interfractional HDR CT images facilitating dose mapping. To the best of our knowledge, this work is the first attempt to incorporate applicator segmentation and removal into the DIR framework for HDR CT images. It is expected that the proposed method will provide the basis for improving patient therapeutic outcome through accurate HDR dose accumulation and dose re-optimization.

In SPEED, we employ the semi-automatic segmentation algorithm, the random walks, for applicator segmentation. The reason of choosing random walks over other fully automatic segmentation algorithms is mainly because of its user-interactive capability. When a failed segmentation result is obtained, it is usually difficult to fine-tune the result using the automatic approaches. In contrast, the random walks can provide a friendly way to adapt segmentation result by simply adding or deleting unsatisfactory seed points (Grady 2005, Grady *et al* 2005, Grady 2006). This merit allows room for emendation for potential segmentation error. Furthermore, in order to minimize user interaction, the foreground and background seed points for random walks are generated automatically via growth on a probability map estimated through a few user-labeled points. This scheme greatly enhances the performance of random walks in that seed points are generated automatically instead of labeled manually and carefully to cover as much intensity levels as possible in an inhomogeneous target. To note that, nevertheless, segmentation error is intrinsic for almost all the automatic and semi-automatic segmentation algorithms, and therefore, the computed AR segmentation should be carefully examined and modified if necessary before it is applied in SPEED. On the other hand, an accurate segmentation method can greatly reduce the workload and labor for revising the computed segmentation. In this sense, the robust AR segmentation performance that has been accomplished in this work is essentially a practical gain of SPEED for its clinical applications.

Another key reason for the success of SPEED is the introduction of the TPS-RPM for AR cavity surface points matching, as well as the initial DVF approximation prior Demons-based

DIR. As we mentioned in the Introduction section, the applicator geometry and position may vary dramatically between fractional insertions, even though Demons is renowned for its capability for handling large deformations, our results showed that it is unable to register the tandem tips of the applicators (section 3.3). Moreover, the sharp dose gradient ($5 \sim 12\%\,\mathrm{mm}^{-1}$) neighboring AR in intracavitary brachytherapy makes it is less forgiving to DIR errors there. In SPEED, a feature-based TPS-RPM algorithm is utilized to obtain the point-to-point correspondence of the two segmented AR cavity surface, and the resulting mapping characteristic of fractional AR surfaces deformation is used to approximate an initial DVF defined on each voxel for subsequent Demons-based DIR. This scheme generally facilitates the DIR process in that it lowers the requirement of Demons for handling large deformation, particularly in those regions where DIR accuracy needs to be emphasized.

In the seed-points auto-generation step, the threshold p_T controlling the FPs growth is empirically chosen. Theoretically, larger p_T implies stricter growing condition. Note, however, that p_T is not the only factor contributing to the FPs generation. Connectivity of voxels in the probability map p_i is another factor, which is purely relative to the textural characteristics of the image. According to our observation, although satisfactory segmentation performances can be obtained when smaller p_T is used, we still employ a relatively rigorous $p_T = 0.9$ to filter out those points with high similarity to the user-labeled FPs and include them into the FPs chain. This value is not necessarily to be optimal and more sophisticated methods, e.g. adaptive approaches, need to be investigated in future work.

A synthetic dataset with realistic fractional deformation based on a clinical HDR CT image of a gynecologic cancer patient was developed and used for the evaluation of SPEED. We have generated the deformation as close as possible to the real HDR fractional changes such that rigid and deformable transformations are simulated in the tissues while only rigid transformation is mimicked in the AR.

One limitation of this work is the lack of a physical deformable phantom to confirm the findings presented here. In fact, such a physical phantom for this purpose is being developed in our institute in parallel with the current research. We are building a realistic 3D phantom that consists of anatomies from a HDR CT image of a gynecological cancer patient, and different organs inside the phantom are molded using the 3D printing technique with the contoured anatomies. The phantom is made up of different mixtures of polyvinyl chloride and softener dioctyl terephthalate, in order to mimic different tissue densities and deformations. Crafty phantom design is being investigated to allow for accommodation of landmarks and dosimeters, and insertions of different types of applicators. The applicator insertion in the clinic is a very sophisticated procedure and fractional applicator position change might not be simply modeled as a rigid transformation. Furthermore, it is also challenging to quantitatively investigate the impact of applicator on DIR. This phantom should be carefully designed such that applicator withdrawal only induces negligible neighboring structural deformations, and fiducial marker implant is also needed for deformation benchmarking. In this way, DVF difference in regions surrounding the AR calculated via DIR with and without applicator can be quantified. Also, the imaging quality, material elasticity, reproducibility, tissue characterizations, etc regarding this phantom need to be explored extensively before it can be used for DIR performance evaluation. We would like to include this phantom study into our future work.

Acknowledgments

This work is supported in part by the National Natural Science Foundation of China (no 30970866 and no 81301940). The preliminary results of this work were presented in the 2014

American Brachytherapy Society (ABS) Annual meeting as a 'Top Four Abstract-Best in Physics' outstanding abstract (Zhen *et al* 2014).

References

Anderson C, Lowe G, Wills R, Inchley D, Beenstock V, Bryant L, Chapman C and Hoskin P J 2013 Critical structure movement in cervix brachytherapy *Radiother. Oncol.* **107** 39–45

Canny J 1986 A computational approach to edge detection *IEEE Trans. Pattern Anal. Mach. Intell.* **PAMI-8** 679–98

Christensen G E *et al* 2001 Image-based dose planning of intracavitary brachytherapy: registration of serial-imaging studies using deformable anatomic templates *Int. J. Radiat. Oncol. Biol. Phys.* **51** 227–43

Chui H and Rangarajan A 2003 A new point matching algorithm for non-rigid registration *Comput. Vis. Image Understand.* **89** 114–41

Crum W R, Hartkens T and Hill D L 2004 Non-rigid image registration: theory and practice *Br. J. Radiol.* **77** S140–53

Dalton S and Bell N 2012 CUSP: A C++ templated sparse matrix library (http://cusplibrary.github.io/)

Gao S, Zhang L, Wang H, de Crevoisier R, Kuban D D, Mohan R and Dong L 2006 A deformable image registration method to handle distended rectums in prostate cancer radiotherapy *Med. Phys.* **33** 3304–12

Godley A, Ahunbay E, Peng C and Li X A 2009 Automated registration of large deformations for adaptive radiation therapy of prostate cancer *Med. Phys.* **36** 1433–41

Grady L 2005 Multilabel random walker image segmentation using prior models *Computer Vision and Pattern Recognition, 2005. CVPR 2005. IEEE Computer Society Conf.* (*20–25 June 2005*) vol 1 pp 763–70

Grady L 2006 Random walks for image segmentation *IEEE Trans. Pattern Anal. Mach. Intell.* **28** 1768–83

Grady L, Schiwietz T, Aharon S and Westermann R 2005 Random walks for interactive organ segmentation in two and three dimensions: implementation and validation *Med. Image Comput. Comput. Assist. Interv.* **8** 773–80 (PMID:16686030)

Grigsby P W, Georgiou A, Williamson J F and Perez C A 1993 Anatomic variation of gynecologic brachytherapy prescription points *Int. J. Radiat. Oncol. Biol. Phys.* **27** 725–9

Gu X, Dong B, Wang J, Yordy J, Mell L, Jia X and Jiang S B 2013 A contour-guided deformable image registration algorithm for adaptive radiotherapy *Phys. Med. Biol.* **58** 1889–901

Gu X, Pan H, Liang Y, Castillo R, Yang D, Choi D, Castillo E, Majumdar A, Guerrero T and Jiang S B 2010 Implementation and evaluation of various demons deformable image registration algorithms on a GPU *Phys. Med. Biol.* **55** 207–19

Han K, Milosevic M, Fyles A, Pintilie M and Viswanathan A N 2013 Trends in the utilization of brachytherapy in cervical cancer in the United States *Int. J. Radiat. Oncol. Biol. Phys.* **87** 111–9

Holden M 2008 A review of geometric transformations for nonrigid body registration *IEEE Trans. Med. Imaging* **27** 111–28

Hsu W M, Hughes J F and Kaufman H 1992 Direct manipulation of free-form deformations *SIGGRAPH Comput. Graph.* **26** 177–84

Huger S, Graff P, Harter V, Marchesi V, Royer P, Diaz J C, Aouadi S, Wolf D, Peiffert D and Noel A 2013 Evaluation of the block matching deformable registration algorithm in the field of head-and-neck adaptive radiotherapy *Phys. Med.* **30** 301–8

Kim J *et al* 2013 A novel approach for establishing benchmark CBCT/CT deformable image registrations in prostate cancer radiotherapy *Phys. Med. Biol.* **58** 8077–97

Lee S, Wolberg G and Shin S-Y 1997 Scattered data interpolation with multilevel B-splines *IEEE Trans. Vis. Comput. Graph.* **3** 228–44

Murphy M J, Salguero F J, Siebers J V, Staub D and Vaman C 2012 A method to estimate the effect of deformable image registration uncertainties on daily dose mapping *Med. Phys.* **39** 573–80

Nithiananthan S, Schafer S, Mirota D J, Stayman J W, Zbijewski W, Reh D D, Gallia G L and Siewerdsen J H 2012 Extra-dimensional demons: a method for incorporating missing tissue in deformable image registration *Med. Phys.* **39** 5718

Pace D F, Aylward S R and Niethammer M 2013 A locally adaptive regularization based on anisotropic diffusion for deformable image registration of sliding organs *IEEE Trans. Med. Imaging* **32** 2114–26

Paquin D, Levy D and Xing L 2009 Multiscale registration of planning CT and daily cone beam CT images for adaptive radiation therapy *Med. Phys.* **36** 4

Pearce A, Craighead P, Kay I, Traptow L and Doll C 2009 Brachytherapy for carcinoma of the cervix: a canadian survey of practice patterns in a changing era *Radiother. Oncol.* **91** 194–6

Rogelj P and Kovacic S 2006 Symmetric image registration *Med. Image Anal.* **10** 484–93

Rueckert D, Sonoda L I, Hayes C, Hill D L, Leach M O and Hawkes D J 1999 Nonrigid registration using free-form deformations: application to breast MR images *IEEE Trans. Med. Imaging* **18** 712–21

Sabater S, Andres I, Sevillano M, Berenguer R, Machin-Hamalainen S and Arenas M 2013 Dose accumulation during vaginal cuff brachytherapy based on rigid/deformable registration versus single plan addition *Brachytherapy* **13** 343–51

Salguero F J, Saleh-Sayah N K, Yan C and Siebers J V 2011 Estimation of 3D intrinsic dosimetric uncertainties resulting from using deformable image registration for dose mapping *Med. Phys.* **38** 343

Shi F, Fan Y, Tang S, Gilmore J, Lin W and Shen D 2009 Brain tissue segmentation of neonatal MR images using a longitudinal subject-specific probabilistic atlas *Proc. Soc. Photo Opt. Instrum. Eng.* **7259** 725942–8 (PMCID:PMC2857333)

Trimble E L, Harlan L C, Gius D, Stevens J and Schwartz S M 2008 Patterns of care for women with cervical cancer in the United States *Cancer* **113** 743–9

Vasquez Osorio E M, Hoogeman M S, Teguh D N, Al-Mamgani A, Kolkman-Deurloo I K, Bondar L, Levendag P C and Heijmen B J 2011 3D dose addition of external beam radiotherapy and brachytherapy for oropharyngeal patients using nonrigid registration *Int. J. Radiat. Oncol. Biol. Phys.* **80** 1268–77

Wang H, Dong L, O'Daniel J, Mohan R, Garden A S, Ang K K, Kuban D A, Bonnen M, Chang J Y and Cheung R 2005 Validation of an accelerated 'demons' algorithm for deformable image registration in radiation therapy *Phys. Med. Biol.* **50** 2887–905

Xie Y, Chao M and Xing L 2009 Tissue feature-based and segmented deformable image registration for improved modeling of shear movement of lungs *Int. J. Radiat. Oncol. Biol. Phys.* **74** 1256–65

Yang D, Chaudhari S R, Goddu S M, Pratt D, Khullar D, Deasy J O and El Naqa I 2009 Deformable registration of abdominal kilovoltage treatment planning CT and tomotherapy daily megavoltage CT for treatment adaptation *Med. Phys.* **36** 329

Yang J 2011 The thin plate spline robust point matching (TPS-RPM) algorithm: a revisit *Pattern Recognit. Lett.* **32** 910–8

Zhen X, Chen H, Yan H, Zhou L, Mell L, Yashar C M, Jiang S B, Jia X, Gu X and Cervino L 2014 A deformable image registration method for dose accumulation between HDR CT images *Brachytherapy* **13** S15–S6

Zhen X, Gu X, Yan H, Zhou L, Jia X and Jiang S B 2012 CT to cone-beam CT deformable registration with simultaneous intensity correction *Phys. Med. Biol.* **57** 6807–26

Zhen X, Yan H, Zhou L, Jia X and Jiang S B 2013 Deformable image registration of CT and truncated cone-beam CT for adaptive radiation therapy *Phys. Med. Biol.* **58** 7979–93

Zhou W, Bovik A C, Sheikh H R and Simoncelli E P 2004 Image quality assessment: from error visibility to structural similarity *IEEE Trans. Image Process.* **13** 600–12

Zijdenbos A P, Dawant B M, Margolin R A and Palmer A C 1994 Morphometric analysis of white matter lesions in MR images: method and validation *IEEE Trans. Med. Imaging* **13** 716–24